Characteristics of large-scale and superstructure motions in a turbulent boundary layer overlying complex roughness

ARTICLE TEMPLATE

Characteristics of Large-Scale and Superstructure Motions in a Turbulent Boundary Layer Overlying Complex Roughness

Julio M. Barros[a*] and Kenneth T. Christensen[b]

[a]Fluid Mechanics Unit, Okinawa Institute of Science and Technology, Okinawa, Japan;
[b]Department of Aerospace & Mechanical Engineering, Department of Civil & Environmental Engineering & Earth Sciences, University of Notre Dame, Notre Dame, IN USA and International Institute for Carbon-Neutral Energy Research (WPI-I2CNER), Kyushu University, Fukuoka, Japan

ABSTRACT
The structural attributes of turbulent flow over a complex roughness topography are explored using high-frame-rate stereo particle-image velocimetry measurements in the wall-normal–spanwise plane. The roughness under consideration was replicated from a turbine blade damaged by deposition of foreign materials and contains a broad range of topographical scales arranged in a highly irregular manner. Previous results from Barros and Christensen [1] revealed strong spanwise heterogeneity in the flow attributed to the formation of roughness-induced turbulent secondary flows identified by spanwise-alternating low- and high-momentum flow pathways (HMP & LMP, respectively) in the mean flow marked by enhanced Reynolds stresses and turbulent kinetic energy. Frequency spectra of streamwise velocity at fixed wall-normal location presented herein also display strong dependence on spanwise position. In particular, the roughness promotes enhanced energy content of the large-scale and smaller-scale motions (as opposed to very-large-scale ones). Depending on spanwise position, pre-multiplied spectra highlight significant modification of the energy content of the very large-scale motions (superstructures) due to roughness compared to smooth-wall flow. Of note, a shift in both TKE and RSS content to shorter streamwise scales at an LMP was noted, while less of an impact was found coincident with an HMP.

1. Introduction

The surface conditions encountered in many technologically-relevant flow systems, from internal flows, such as oil and gas pipelines, to external flows, such as turbine blades, ship hulls, wind turbines and heat exchangers, can deteriorate over time due to multiple damage mechanisms that generate irregular surface features embodying a broad range of scales. Roughness can directly degrade the performance of these flow systems, leading to increased drag and heat transfer loads at the surface. Many efforts have studied the impact of surface roughness on wall turbulence, with most of these

efforts employing simplified idealized roughness, such as sand grain, woven mesh and 2D roughness elements ordered in a regular fashion. Although these idealized form of roughness are relatively easy to implement in laboratory experiments, they may not necessarily reflect the full richness of practical roughness. For instance, surfaces of turbine blades suffer cumulative damage over their lifetime due to different damage mechanisms, such as deposition of foreign materials, pitting and spallation of the thermal barrier coating, all of which are marked by the generation of a broad range of topographical scales. It is crucial to establish a deeper understanding of the impact of more realistic roughness on the turbulent characteristics of wall-bounded flows, including how it alters the structural characteristics of smooth-wall flow.

The large- and very-large-scale motions of smooth-wall turbulence have been heavily investigated over the last several decades owing to their importance in momentum and energy transport. In early works by Townsend [2] and Grant [3], they identified the presence of large-scale motions (LSMs) from the long tails of time-delayed streamwise velocity, u', auto-correlations that extended to 1.4δ, where δ is the boundary-layer thickness. These works also concluded that these LSMs carry a significant fraction of the turbulent kinetic energy (TKE). Recent studies have postulated these LSMs to be associated with the coherent alignment of hairpin-like vortices into δ-scale vortex packets as identified by Adrian et al. [4]. Kim and Adrian [5] showed that premultiplied streamwise velocity spectra at the lower edge of the logarithmic layer in pipe flow has a bimodal distribution, displaying a peak at a "low" wavenumber (associated with the energy content of very-large-scale motions, VLSMs) and a secondary peak at a higher wavenumber (associated with LSMs), that are consistently present for a range of Reynolds numbers (Re). They also found that the wavelength of the VLSMs can extend to as large as 12-14 times the pipe radius, that they embody a significant fraction of TKE and conjectured that VLSMs are perhaps due to a coherent streamwise ordering of LSMs. Guala et al. [6] extended the work of Kim and Adrian [5], showing that VLSMs are not only energetic, containing as much as 50% of the TKE of the streamwise velocity component, but also account for more than half of the RSS, $\langle u'v' \rangle$ (where v' is the wall-normal velocity fluctuation). Balakumar and Adrian [7] performed hot-wire measurements in both channel and TBL flows for a wide range of Re and found that such motions in both flows carry a significant fraction of the streamwise component of the TKE (40-65%) and RSS (30-50%), similar to the results of Guala et al. [6] in turbulent pipe flow. Other recent efforts have identified differences in the VLSM characteristics in internal and external turbulent flows [8].

These VLSMs, also termed 'superstructures' in the turbulent boundary layer (TBL) literature to distinguish from the VLSM terminology in internal flows (pipes and channels), are known to persist under realistic scenarios, such as the atmospheric TBL, whose Re can be three orders of magnitude higher than laboratory conditions [9,10]. Hutchins and Marusic [10] used a spanwise rake of hot-wire sensors to reconstruct streamwise-elongated fields of view from time traces of u' which revealed the spatial signatures of superstructures. These reconstructed fields embodied spanwise-meandering regions of streamwise momentum deficit ($u' < 0$) that extended several δ in the streamwise direction, with a characteristic spanwise width of approximately 0.4δ. Marusic and co-workers have also reported evidence that such spatial scales have a clear footprint in the inner layer and modulate the smaller-scale motions in the near-wall region [11,12]. In particular, Mathis et al. [11] applied a scale-decomposition on time series of streamwise velocity fluctuations, extracted the large-scale signature of these series, applied the Hilbert transform to the small-scale signals and extracted its large-scale envelope. By correlating the large-scale signature with the large-scale envelope

2

of the small scales, they were able to identify significant levels of correlation that signified this amplitude modulation effect in a manner similar to that identified by Bandyopadhyay and Hussain [13].

The impact of roughness on the aforementioned structural skeleton of smooth-wall flow is not yet fully understood, but recent studies have identified similarities between smooth- and rough-wall flow that indicate the underlying structure to be qualitatively similar. Related to this is the possibility that the outer layer of rough-wall flow is not directly impacted by roughness but rather equilibrates to the δ and wall shear stress set by the roughness in a universal way. Known as Townsend's outer-layer similarity hypothesis, it is not known whether this notion holds at the scales of the LSMs and VLSMs. Krogstad et al. [14] performed hot-wire measurements in a TBL over wire mesh (k-type roughness; $\delta/k = 50$). The authors reported small differences between the smooth and rough-wall flows in the both streamwise velocity spectra, ϕ_{uu}, and the co-spectra, ϕ_{uv}, but significant differences in the wall-normal velocity spectra, ϕ_{vv}. This latter difference was found to exist at all wave numbers for two wall-normal positions in the outer layer ($y/\delta = 0.1$ and 0.4). Krogstad and Antonia [15] then investigated differences between two types of roughness (woven mesh, $\delta/k = 50$, and 2D rods, $\delta/k = 47$) as compared to smooth-wall flow, and they identified similar trends for the velocity spectra in the outer layer as reported by Krogstad et al. [14]. Although the aforementioned works identified alterations (small, but present) in the streamwise velocity spectra, their results also showed a distinctive peak in the premultiplied form of spectra at $k_x\delta \approx 2$ ($\lambda_x/\delta \approx 3$), which inferentially supports the presence of LSMs in the outer layer, similar to smooth-wall flow [5–7].

Volino et al. [16] observed spatial signatures of hairpin vortex packets in instantaneous PIV velocity fields in wall-normal ($x - y$) and wall-parallel ($x - z$) planes of a TBL over woven wire mesh (3D roughness). Two-point correlations of streamwise velocity showed a slight reduction in streamwise spatial coherence of the flow close to the wall, compared to smooth-wall flow, that rapidly diminished with increasing wall-normal position. Similar trends were observed by Wu and Christensen [17], where they reported outer-layer similarity in two-point spatial velocity correlations for flow over the same complex roughness employed herein based on PIV measurements in the $x - y$ plane. Wu and Christensen [18] subsequently reported that complex roughness altered the characteristic streamwise and, to a lesser extent, the spanwise length scales of the flow based on stereo PIV measurements in a wall-parallel plane near the outer edge of the roughness sublayer ($y \approx 0.2\delta$ relative to the mean elevation of the roughness). Nevertheless, this rough-wall flow was still found to embody many of the structural attributes of hairpin vortex packets, including elongated LMRs bounded by wall-normal vortex cores interpreted as slices through the legs/necks of hairpin vortices. Interestingly, Volino et al. [19] found that 2D, k-type roughness (transverse square bars; $\delta/k = 32$) had a markedly different and significant impact on the spatial scales of the flow in both the near-wall and outer regions of the flow. Two-point correlations of streamwise velocity showed an increase of approximately 40% in streamwise extent, 40% increase in wall-normal extent and 10-15% increase of spanwise extent when compared with both smooth-wall and rough-wall flow over 3D roughness. It was argued that, while 3D roughness elements generate structures of size comparable to k, 2D roughness generates larger structures due to the increased spanwise width of the roughness elements.

Allen et al. [20] reported streamwise velocity spectra measured deep within the log layer of a transitionally-rough turbulent pipe flow that agreed well with smooth-wall flow, indicating little modification of the underlying turbulence structure. Monty

et al. [21] reported streamwise velocity spectra for flow over braille dots that collapsed at smaller scales in the outer region with smooth-wall data, in accordance with Townsend's similarity hypothesis. At larger scales ($\lambda_x/\delta \approx 6$) at higher Re in the log region, they reported reductions in the energy content which suggests the possibility of manipulating LSMs and VLSMs in the presence of regular roughness. Similar modification of the energy content of the larger scales was reported by Jacobi and McKeon [22], but for a vastly different roughness scenario: a single impulse of 2D roughness in a TBL. Discrepancy maps of streamwise velocity spectra ('perturbed' relative to 'smooth') a few roughness heights downstream of the roughness impulse showed significant LSM and VLSM suppression up to the wall-normal height of the roughness perturbation. Similar modifications of the larger-scale energy content was achieved using a single circular cylinder element immersed into the log layer of turbulent channel flow [23]. While these studies only considered spatially-compact roughness perturbations, they clearly suggest the possibility of altering the energy content of flow scales much larger than the roughness itself.

In our previous efforts [1,24], it was shown that roughness embodying a broad range of topographical scales induces spanwise heterogeneities in the mean flow in the form of spanwise-localized low- and high-momentum pathways (LMPs and HMPs, respectively) [size of order δ] that are flanked by streamwise-oriented counter-rotating vortex pairs. These patterns are consistent with the existence of roughness-induced turbulent secondary flows and Anderson et al. [25] found that such spanwise topographical heterogeneity induces such turbulent secondary flows of the second kind that are driven by spatial gradients in the Reynolds-stress components, causing an imbalance between the production and dissipation of turbulent kinetic energy, which requires secondary advection velocities to be present. This is associated with high surface stress on relatively high-roughness regions coupled with elevated turbulence production in the fluid immediately above. Barros and Christensen [1] presented the spatial relationships between the spanwise variation in the roughness height and the occurrence of LMPs, HMPs and swirling motions in the flow-normal plane of a TBL overlying complex roughness. Figure 1(a) shows the ensemble-averaged mean velocity field with the in-plane mean velocity components shown as vectors to complement the mean streamwise velocity shown as contours. A spanwise roughness profile, $\eta(z)$, is shown beneath the mean velocity field and represents the streamwise-averaged topographical height over a δ-long streamwise fetch immediately upstream of the measurement location. It can be seen that there exist clear imprints of swirling motions in the mean flow bounding the LMPs identifiable in the mean streamwise velocity contours. Comparing the spanwise positions of the LMP and HMP features with the spanwise variation in the low-pass-filtered roughness height to accentuate larger-scale variations in the roughness height [shown beneath the mean velocity field in figure 1(a) as a black line], it appears that the HMPs tend to sit at spanwise positions of relatively elevated topography while the LMPs tend to reside at spanwise positions of relatively recessed topography. The occurrence of such mean-flow heterogeneities has also been identified in flow over other roughness topographies [26–29].

Finally, hot-wire measurements by Pathikonda and Christensen [30] in flow over the same complex roughness used by Barros and Christensen [1] identified the suppression of the near-wall peak in pre-multiplied streamwise velocity spectra normally observed in smooth-wall flow at the spanwise locations of both LMPs and HMPs. They also noted persistence in VLSM-scale energy in the flow at LMPs, though a slight shift towards shorter streamwise wavelengths was observed, while the energy content at HMPs embodied slightly weaker energy at VLSM scales as well as additional energy

4
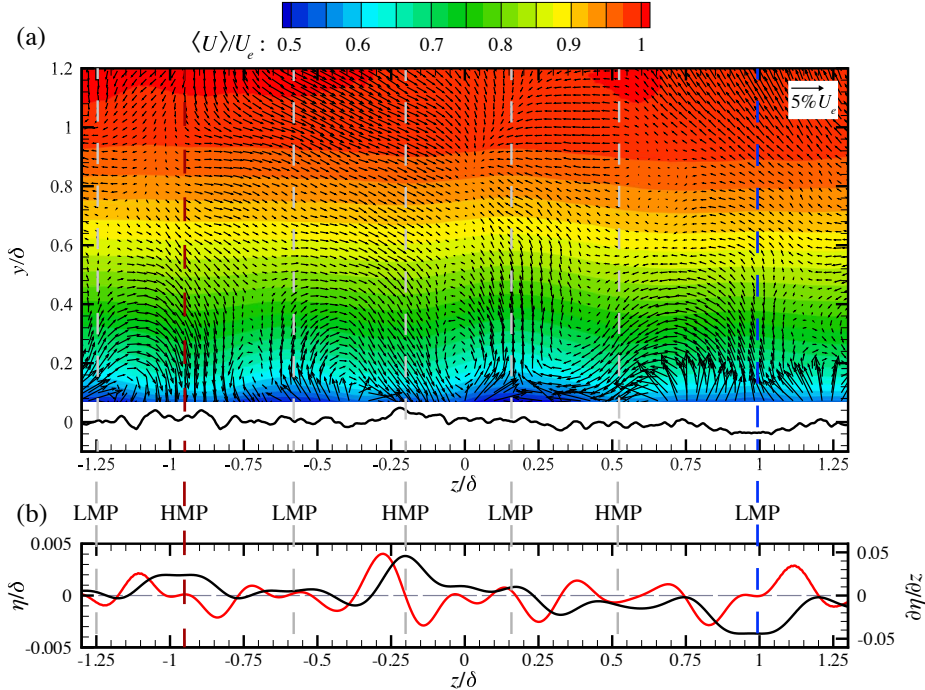
Figure 1. (a) Mean velocity field (contours: $\langle U \rangle$; vectors: $\langle V \rangle$ and $\langle W \rangle$) with the spanwise roughness profile averaged over a δ-long fetch upstream of the measurement plane shown below the field (Scaled by a factor of five). Flow is into the page. (b) Low-pass-filtered spanwise roughness profile (black line) and its spanwise gradient (red line). Adapted from Barros and Christensen [1]. Blue and red dash lines show the identified LMP and HMP, respectively, used in the results section.

at more intermediate streamwise scales ($\lambda_x \sim \delta$). Awasthi and Anderson [31] also considered modifications of premultiplied streamwise velocity spectra calculated from large-eddy simulations (LES) of flow over a more ordered, yet spanwise-varying, topography that yielded secondary flows. They also observed preservation of energy at VLSMs at LMPs, though with a shift towards lower streamwise wavelengths, and reported additional evidence that such structures are indeed shorter and steeper. However, in contrast to that noted by Pathikonda and Christensen [30], their results over a more ordered, spanwise-varying topography suggested an annihilation of VLSMs at HMPs, which they attributed to vigorous mixing identified in the outer layer at HMPs.

The focus of the current effort is to study characteristics of LSMs and super-structures in a TBL overlying complex roughness which embodies the aforementioned roughness-induced turbulent secondary flows. In particular, we seek to understand the behavior of LSMs and VLSMs as a function of spanwise position, particularly their characteristics at spanwise locations coincident with LMPs and HMPs. To this end, high-frame-rate stereo PIV data in the same cross-flow plane as Barros and Christensen [1] was acquired to assess the localized impact of highly irregular roughness within the roughness sublayer on LSMs and superstructures in a TBL. Two types of experiments were performed: (1) a large field-of-view at 1.5k field/s that provides a view of the overall spatial structure across the boundary layer, and (2) a narrow wall-normal measurement strip at 10k fields/s, which would equate to having a rake of roughly 1000 triple-wire sensors simultaneously acquiring all three velocity components. The 10k fields/s measurements reported herein were performed at the same Re as the low-frame-rate cross-plane stereo PIV measurements from Barros and Christensen [1], ensuring the same flow scenario/conditions under which the aforementioned

Table 1. Summary of the roughness statistics.

k [mm]	k_a [mm]	k_{rms} [mm]	Sk	Ku	l_{corr_x} [mm]	l_{corr_z} [mm]
4.25	0.63	1.00	0.16	2.28	6.93	5.51
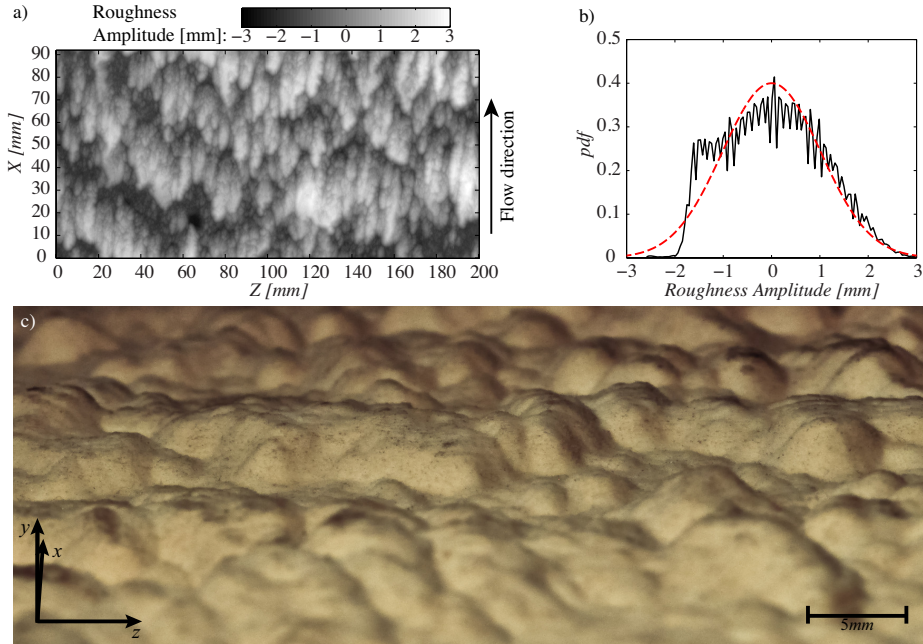
Figure 2. (a) Topographical map of the roughness. (b) Pdf of roughness height about the mean elevation. (c) Photo of the replicated roughness in the wind tunnel along the flow direction.

turbulent secondary flows were observed. The measurements reported herein complement recent studies that leveraged streamwise velocity statistics for this purpose [30,31] as they capture all three velocity components and thus facilitate evaluation of both the TKE and RSS content of LSMs and VLSMs in the presence of roughness-induced secondary flows.

2.   Experimental Setup

The TBL experiments were conducted in an open-circuit Eiffel-type, boundary-layer wind-tunnel. The test section of the tunnel is 6 m long, 45.7 cm tall and 91.4 cm wide, and all boundary layers were formed on a smooth boundary-layer plate suspended above the bottom wall of the tunnel. This plate consists of two 3-m long and 91.4-cm wide smooth-wall sections smoothly joined at the streamwise center. Zero-pressure-gradient conditions were achieved via an adjustable ceiling in the test section. Previous studies provide a more detailed description of this facility and its flow quality [17,18, 32,33].

The rough surface used was the same as that originally fabricated and studied by Wu and Christensen [17,18]. This surface is a scaled version of a profilometric surface scan of a turbine blade damaged by deposition of foreign materials, which was first reported by Bons et al. [34]. Figure 2(a) presents a topographical map of the rough surface, which is marked by a broad range of topographical scales arranged in an irregular manner. The average peak-to-valley roughness height of this surface is $k =$

6

4.25 mm while the root-mean square (RMS) roughness height, k_{rms}, is 1.0 mm. Table 1 summarizes the roughness statistics, namely, k_a: the absolute mean roughness height, Sk: the roughness skewness, Ku: the roughness kurtosis, and l_{corr_i}: the correlation length in the i direction defined when the correlation peak is equal to $1/e$. As described in Wu and Christensen [18], a 3-m long replica of this topography was achieved by mirroring it in both the streamwise and spanwise directions and fabricated with a powder-deposition printer. This roughness was mounted on cast aluminum plates and placed along the downstream half of the boundary-layer plate by adjusting its height above the bottom wall of the tunnel such that the mean elevation of the roughness was coincident with the upstream smooth-wall conditions. Thus, the boundary layers under study were allowed to initially develop over the first 3 m of the smooth boundary-layer plate followed by an additional 3 m of development over the roughness. In all cases the flow was tripped with a cylindrical rod near the upstream end of the boundary-layer plate and all measurements were conducted approximately 2.3 m downstream of the leading edge of the roughness. Wu and Christensen [17] previously reported this rough-wall flow to have achieved self-similar conditions at this measurement location. Figure 2(c) presents a zoomed-in photo of a portion of the roughness replica in the wind tunnel. This photo highlights the complex, multi-scale nature of the topography. As in the present experiments, the features of these natural topographies typically protrude into the outer (logarithmic) region of the flow but are an order of magnitude smaller than the characteristic flow depth (δ).

Figure 3 presents a schematic of the stereo PIV arrangement utilized for the high-frame-rate experiments. The system consisted of two $1k \times 1k$ pixel, 10-bit, CMOS cameras (Fastcam APX-RS Photron) and a 30 mJ/pulse at 1 kHz, dual-cavity pulsed Nd:YLF laser (Litron). A 1.0 mm thick laser lightsheet was formed by three cylindrical lenses and directed into the tunnel's test section in the $y-z$ plane. The cameras viewed the $y-z$-oriented lightsheet from a forward-scattering perspective to maximize the intensity of the scattered light imaged by the cameras, with one camera upstream to the laser lightsheet and the other downstream of it, through optical-grade glass side-walls of the wind tunnel at angles of $\pm 45°$ from the streamwise (x) direction. In the measurement plane, the angle between each lens and camera CMOS array was adjusted to satisfy the Scheimpflug condition which ensured uniform focus across the field of view. The flow was seeded with $1\,\mu$m olive-oil droplets generated by a Laskin nozzle and timing of the cameras, lasers and image acquisition was controlled with a timing unit with 1 ns resolution.

Accurate stereo PIV measurements required careful calibration of the imaging system to properly map the image coordinate system to the object plane defined by the laser lightsheet. A single-plane target consisting of dots spaced at 2.5 mm in both the horizontal and vertical directions was utilized in the cross-plane experiments. The front face of this target was carefully aligned with the center of the lightsheet. Images of this target were acquired by both cameras at this position as well as with the target translated $\pm 250\,\mu$m upstream and downstream of lightsheet center. The resulting calibration images for each measurement plane were used to generate calibration mapping functions to map the two, 2-D image planes to the 3-D space defined by the laser lightsheet using the least-squares method of Soloff et al. [35]. Thus, the out-of-plane fluid motion was discerned from the distinct views of the tracer-particle motion within the laser lightsheet as imaged by the two cameras for each of the stereo PIV experiments.

In order to study the overall dynamics of the flow in both the roughness sublayer and the outer layer of the rough-wall flow simultaneously, an acquisition rate of 1.5 kHz was utilized. Table 2 summarizes the relevant experimental parameters for these measure-
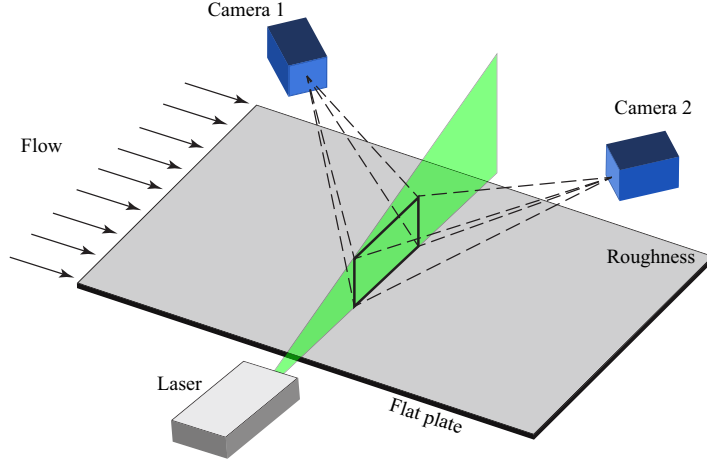
Figure 3. Schematic of the experimental arrangements in the wall-normal–spanwise $(y - z)$ measurement plane for the high frame-rate stereo PIV measurements.

Table 2. Summary of the experimental parameters for the TBL experiments conducted.

Surface	U_e [m/s]	δ [mm]	Re_θ	u_τ [m/s]	δ^+	$k+$	δ/k	F.O.V	Acq. Freq [kHz]	N
Rough	6.0	90.0	4500	0.31	1792	56.1	21.2	$0.8\delta \times 1.3\delta$	1.5	3000
Smooth	17.3	85.3	10000	0.63	3214	-	-	$0.1\delta \times 1.3\delta$	10	21845
Rough	17.5	94.9	13700	0.91	4850	217.2	22.1	$0.1\delta \times 1.3\delta$	10	21845

ments. For reference, the boundary-layer thickness, δ, was taken as the wall-normal location where the mean streamwise velocity, U, was 99% of the free-stream velocity, U_e. Doing so allowed the full 1k × 1k camera array size to be active and will also maximize the laser energy output over this relatively wide field of view (δ-scale). To maintain sufficient time resolution in these measurements so that the evolution of all but the smallest scales of motion (y_*) can be captured, the Re of these 1.5 kHz measurements was somewhat lower than those of the previously described low-frame-rate PIV measurements in this cross-flow plane by Barros and Christensen [1]. Reducing the Re ensured that the streamwise displacement of the flow through the lightsheet between consecutively acquired PIV velocity fields was comparable to the in-plane grid spacing of the PIV fields so that the evolution of the smallest resolved in-plane motions were also resolved in time. These experiments provided a basis for reconstructing the qualitative features of the larger-scale motions across both the roughness sublayer and the outer layer of the flow. Under this scenario, Taylor's hypothesis can be utilized to convert the temporal dimension to equivalent streamwise position assuming that the turbulence is frozen with respect to the advection in the streamwise direction. A single advection velocity was utilized when reconstructing the instantaneous structures based on the bulk velocity of the flow, giving $x \simeq (t_\circ - t)\bar{U}$ [36–38] in a manner consistent with previous hot-wire reconstructions reported by Marusic and co-workers that first revealed the spatial imprints of superstructure events in smooth-wall flow [10,39].

High-frame-rate stereo PIV data in the same cross-flow plane was also acquired at 10 kHz for a field of view that was narrow in the wall-normal direction but wide in the spanwise direction just above the crests of the roughness ($\sim 0.1\delta \times 1.3\delta$; $y \times z$), for both smooth- and rough-wall flows. These measurements were performed at the same higher Re as the aforementioned low-frame-rate cross-plane stereo PIV measurements of Barros and Christensen [1] that identified the turbulent secondary flows over the roughness considered herein. These narrow-strip measurements are unique because

8

they simultaneously resolve all three components of velocity at 10 kHz at roughly 1000 grid points in the narrow spanwise strip. Such a measurement cannot be achieved with hot-wire sensors (recall that Marusic and co-workers utilized 10 single-wire, hot-wire sensors in a spanwise array in their initial smooth-wall measurements that captured the spatial imprints of superstructures) nor has such a measurement been achieved by PIV. In this way, the frequency spectrum (up to 5 kHz ($F_N^+ = 0.12$ in inner units, where $t^* = \nu/u_\tau^2 = 2.47 \times 10^{-5}$ s) to ensure no aliasing effects) of each velocity component can be simultaneously documented at multiple spanwise and wall-normal positions from a *single* experimental run so that the energy content as a function of scale as well as spanwise and wall-normal position can be studied. Furthermore, since all three velocity components are acquired simultaneously, the full TKE frequency spectrum can be reconstructed at each grid point as can the various co-spectra combinations (particularly that of the RSS, $\langle u'v' \rangle$, which can be utilized to study RSS content as a function of scale as well as spanwise and wall-normal position). Of particular interest herein was documenting how complex roughness alters the scale distribution of TKE and RSS energy content, and how it might drive spanwise dependence of TKE and RSS energy content across different scales of the flow.

For all cases, each instantaneous three-component velocity field was derived from two, 2-D displacement fields generated from the time-delayed pairs of images acquired by each camera. These pairs of time-delayed images were interrogated using a recursive, two-frame cross-correlation methodology. The first-pass interrogation was performed with a bulk window offset to minimize loss of particle pairs, while the final-pass interrogation was performed with square interrogation spots of size 16^2 pixels with 50% overlap to satisfy the Nyquist sampling criterion, and the second window was locally offset by an integer pixel displacement determined during the first-pass interrogation. Statistical validation tools were employed between passes to identify and replace erroneous vectors as well as after the final interrogation pass was completed, including Rohaly–Hart [40] replacement with displacements assessed from alternate correlation peaks identified during the interrogation process. All fields were then low-pass filtered with a narrow Gaussian filter to remove high-frequency noise. Each pair of 2D displacement fields was then recombined using the aforementioned mapping function to reconcile all three instantaneous velocity components on the measurement plane defined by the laser lightsheet.

The final field of view for the 1.5 kHz cases was $0.8\delta \times 1.3\delta$ (wall-normal by spanwise), and $0.1\delta \times 1.3\delta$ for the 10 kHz cases. In all cases, the grid spacing achieved was $680\,\mu$m in both spatial directions. The record length, T, was $\approx 140 t_h$ for the 1.5 kHz case and $\approx 400 t_h$ for the 10 kHz case, where t_h is the eddy turnover time, $t_h = \delta/U_e$.

3. Results

3.1. *Instantaneous Structure*

Figure 4(a) presents a representative instantaneous fluctuating velocity field in the $y - z$ measurement plane for the rough-wall case acquired at 1.5 kHz, providing a wall-normal view that embodies nearly the entire boundary-layer thickness. The velocity fluctuations were calculated from the ensemble-averaged velocity field (represented by the overline), $\overline{U_i}(y,z)$ $[u'_i(y,z,t) = U_i(y,z,t) - \overline{U_i}(y,z)]$, where $U_i(y,z,t)$ is the ith component of instantaneous velocity. The in-plane wall-normal (v') and spanwise (w') velocity fluctuations are shown as vectors and the out-of-plane streamwise ve-
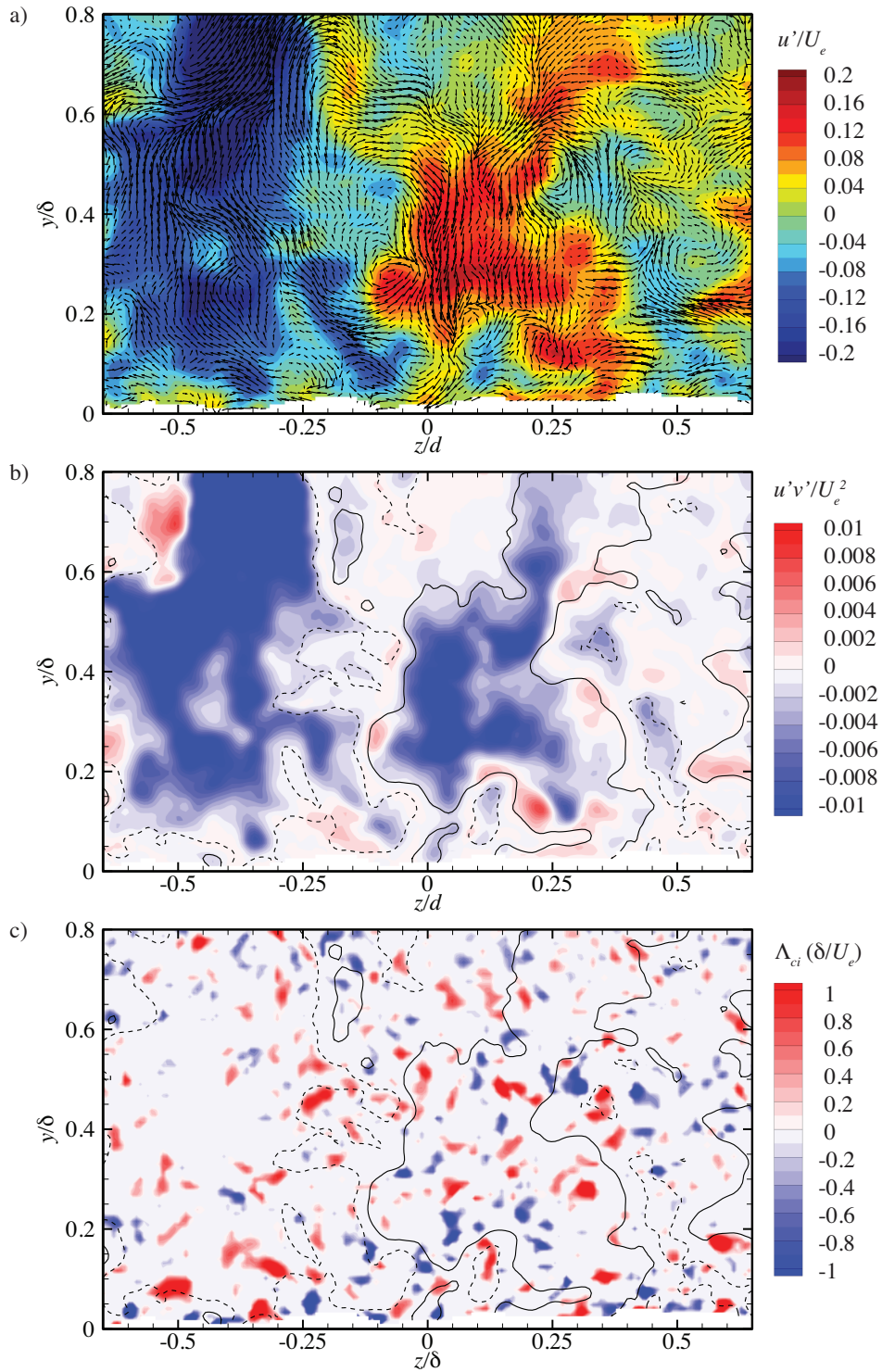
Figure 4. (a) Representative instantaneous fluctuating velocity field in the $y - z$ plane from the $1.5\,\mathrm{kHz}$ rough-wall data (contours: u'; vectors: v', w'). Contours of (b) instantaneous contributions to the RSS, $u'v'$, and (c) signed swirling strength, Λ_{ci} for field in (a). Solid and dashed line contours in (b) and (c) demarcate boundaries of HMRs and LMRs, respectively.

10

locity fluctuations (u') are presented as background contours. Note that the positive streamwise (x) direction, and hence the mean flow, is *into* figure 4(a). The streamwise velocity fluctuations are marked by large (δ-scale) regions of low and high instantaneous streamwise momentum that appear to alternate in the spanwise direction with a spacing of $\sim 0.5\delta$. These patterns are interpreted as the cross-plane signatures of the LMRs and HMRs and can often extent to the edge of the boundary layer. These instantaneous features are well-documented in both smooth- and rough-wall flow and are entirely separate from the aforementioned HMP and LMP spanwise flow heterogeneities identified in the mean flow over this roughness owing the occurrence of roughness-induced turbulent secondary flows. Focusing upon the large-scale LMR near $z = -0.2\delta$ in figure 4(c), its left boundary is populated by counter-clockwise-rotating vortex cores identified with signed swirling strength ($\Lambda_{ci} < 0$; blue) while its right boundary is populated by vortex cores with clockwise rotation ($\Lambda_{ci} > 0$; red). Furthermore, rather intense, positive wall-normal velocity fluctuations (v') are observed within this LMR, resulting in a large-scale region of low-speed fluid ejected away from the wall which contributes heavily to the mean RSS (Figure 4b). This LMR is flanked on its spanwise boundaries by HMRs within which intense, negative v' create a large-scale sweep of high-speed fluid towards the wall which also contributes heavily to the mean RSS (Figure 4b). Apart from these δ-scale events, smaller LMRs and HMRs are visualized in the near-wall region that are often bounded by streamwise vortex cores. These smaller-scale regions appear to co-exist beneath the larger-scale LMRs and HMRs, supporting the contention that such structures occur in a hierarchy of scales across the flow. As proposed by Adrian et al. [4] for smooth-wall turbulence, packets of varying size would be expected throughout the wall-normal extent of the flow, with smaller, younger, slower packets residing closer to the wall where they are likely formed and successively larger, older packets populating the outer region of the flow while maintaining a near-wall footprint. It was shown that many of the structural attributes of the hairpin packet persist in the presence of 3D roughness [16–18,24]. However, their characteristic spatial scales are modified as Wu and Christensen [18] and Mejia-Alvarez and Christensen [32] both found that the roughness employed herein alters the streamwise length scales of the flow. Nevertheless, despite the presence of a rough boundary, the overall structural attributes of the flow are quite consistent, at least qualitatively, with those of smooth-wall turbulence. This observation is in accordance with Townsend's wall similarity hypothesis [41] whereby the roughness sets the wall shear stress and the boundary-layer thickness and the turbulence in the outer region simply adjusts itself to these constraints in a universal manner.

3.2. *Imprints of large- and very-large scale motions in rough-wall flow*

Figure 4 clearly highlights the existence of δ-scale flow features in the cross-flow plane that are consistent with signatures of LSMs and VLSMs in smooth-wall flow. The cross-plane high-frame-rate stereo PIV data affords one the opportunity to also explore the presumed streamwise elongation of these motions in a manner consistent with that often utilized to convert hot-wire time traces to equivalent spatial extent. This exact methodology allowed Hutchins and Marusic [10] to reconstruct spanwise and elongated streamwise fields of view from time series acquired simultaneously from a spanwise rake of 10 hot-wire sensors that led to their observations of spanwise meandering regions of $u' < 0$ that extended multiple δ in the streamwise direction which they termed superstructures (consistent with attributes of VLSMs). As the streamwise
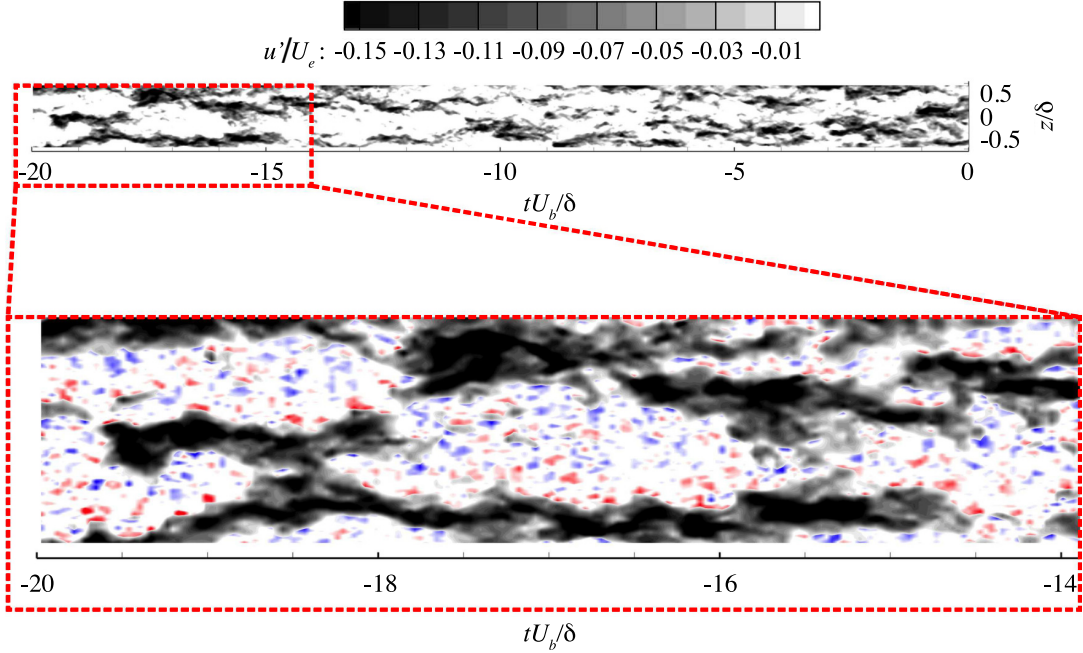
Figure 5. Wall-parallel $(x-z)$ view of an LMR at $y/\delta = 0.15$ demarcated with contours of negative streamwise velocity fluctuation from Taylor's hypothesis reconstruction. A zoomed-in region is also presented with color contours of signed swirling strength demarcating the locations of wall-normal vortex cores.

displacement of the bulk flow between consecutive instantaneous vector fields herein was maintained at half of the lightsheet thickness, consistent with the in-plane spatial resolution, Taylor's hypothesis was utilized to convert the temporal dimension to equivalent streamwise position assuming that the turbulence is frozen with respect to mean advection in the streamwise direction. Here, a single wall-parallel $(x \times z)$ plane was reconstructed in the spirit of that reported in Hutchins and Marusic [10] for smooth-wall flow based on the mean streamwise velocity at this wall-normal position, giving $x \simeq (t_\circ - t)\bar{U}$ [36–38].

Figure 5 presents the result of this Taylor's-hypothesis reconstruction in the wall-parallel $x - z$ plane at $y/\delta = 0.15$ highlighting the presence of an instantaneous LMR demarcated with contours of $u' < 0$. Here several multiple-δ regions of connected $u' < 0$ that have significant spanwise meander are readily apparent in a manner quite reminiscent of that observed by Hutchins and Marusic [10] for smooth-wall flow. A zoomed-in region is also presented with color contours of in-plane signed swirling strength demarcating the locations of wall-normal vortex cores. Focusing upon the zoomed-in region in Figure 5, it is apparent that the streamwise-elongated LMRs are bounded on the spanwise edges by counter-rotating vortex cores in a manner consistent with hairpin vortex packets. In addition, this result highlights the elongated streamwise extent of these superstructures, which appear to extend $5 - 6\delta$ in the streamwise direction, again quite reminiscent of similar patterns reported by Hutchins and Marusic [10] from measurements using a spanwise array of hot-wire sensors in conjunction with Taylor's hypothesis to reconstruct streamwise-elongated, wall-parallel fields of view in a smooth-wall TBL. As already mentioned previously and also shown in the recent work of Wu and Christensen [18], albeit for much shorter streamwise extents (δ), these LMRs are qualitatively similar to the structures found in smooth-wall flow. The present reconstructions, however, show that these LMRs have streamwise extents of multiple

12
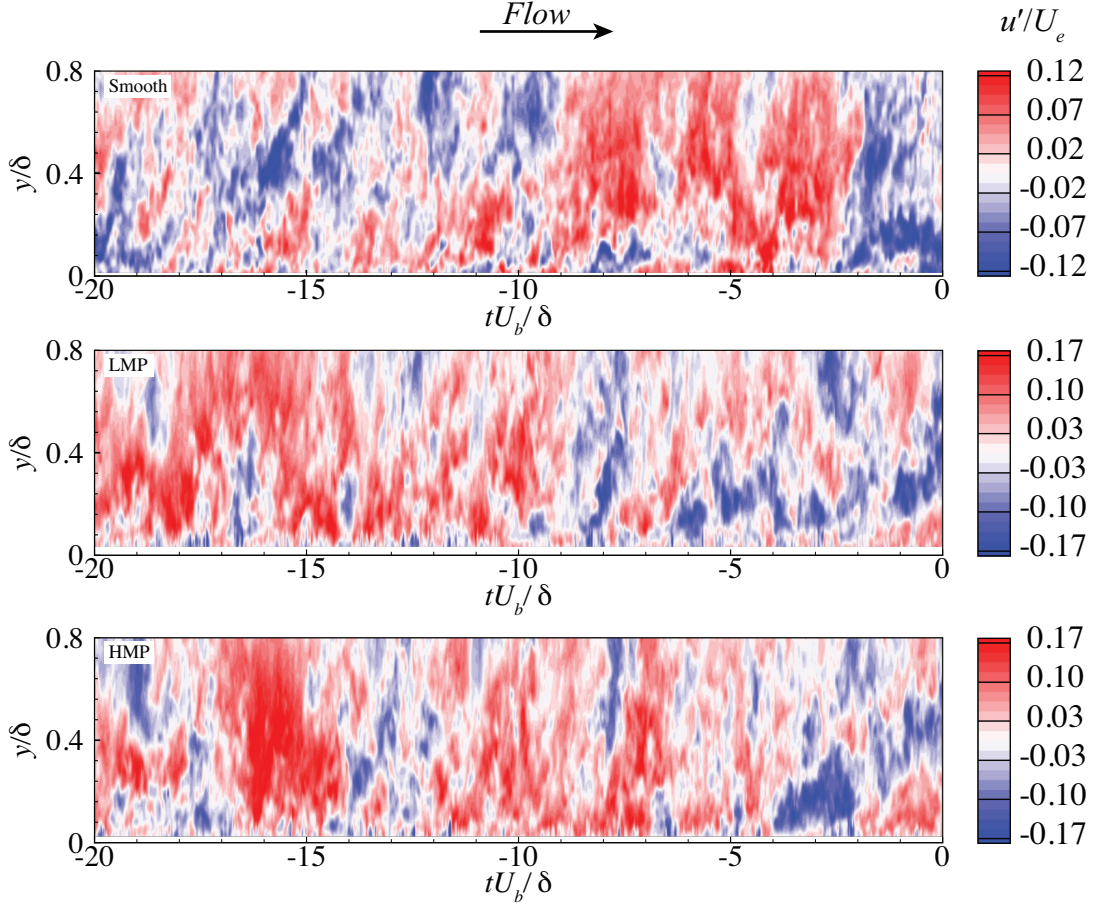
Figure 6. Time-height contours of fluctuating streamwise velocity for a) smooth-wall flow [43], and rough-wall flow at an b) LMP and c) HMP. The time axis is normalized by the bulk velocity and the boundary-layer thickness to give a qualitative sense of the streamwise scales of the different structures identified.

δ and could be the imprint of superstructures previously identified in smooth-wall flow which embody a significant fraction of TKE and RSS. Mejia-Alvarez et al. [42] previously reported the existence of such superstructures in this same rough-wall flow in elongated wall-parallel fields of view constructed by stitching together time-delayed PIV velocity fields acquired in the wall-parallel plane. Despite the limited temporal resolution (1k fields/s) and a narrower spanwise domain (only 0.5δ) the present observations confirm those initially reported by Mejia-Alvarez et al. [42], particularly the existence of streamwise-elongated regions of $u' < 0$ that spanwise meander.

Leveraging the wall-normal extent of the present high-speed data, figure 6 presents a time history of the streamwise velocity fluctuations as a function of wall-normal position for three flows: smooth-wall flow [43] (figure 6a and rough-wall flow at two different spanwise positions: coincident with an LMP (figure 6b) and coincident with an HMP (figure 6c). It should be noted that the smooth-wall from [43] used in this section is from a higher Reynolds number ($Re_\theta = 10000$). Despite this difference, it serves as an effective baseline for the qualitative discussion herein. The time axis is normalized by the cross-plane bulk velocity and δ, allowing the streamwise length scale of flow events to be qualitatively inferred from these time histories, while the wall-normal location is normalized by δ. Only a portion of the high-frame-rate data acquired is presented for clarity.

13

Focussing on the smooth-wall result in figure 6(a), many δ-scale events of LMRs (blue contours; $u' < 0$) and HMRs (red contours; $u' > 0$) alternate along the time axis, all with varying wall-normal extents ranging from $y \approx 0.2\delta$ to 0.8δ. In addition, the inclined nature of these structures away from the wall is readily apparent in this presentation of the time histories, with a characteristic angle of $12 - 17$ degrees. This inclination is consistent with previous studies of smooth-wall turbulence, particularly the typical inclination of hairpin vortex packets [4,44]. The character of the flow as inferred from the time history of u' is somewhat different in the presence of roughness. Figure 6(b) shows the time series of the flow at a spanwise position coincident with an LMP and the same in figure 6(c) at an HMP. For both spanwise positions, the flow is qualitatively distinct from the smooth-wall case, particularly the flow closer to the rough surface ($y/\delta < 0.1$) where easily identifiable small-scale features are present at scales consistent with that of the roughness. In addition, the flow within the roughness sublayer shows significant differences when compared with the smooth-wall case. The structures present along an LMP, depicted in figure 6(b), appear smaller in streamwise extent when compared with the smooth-wall case. Although these features still resemble packet-like structures, some LMRs have rather steep inclination angles compared to smooth-wall flow, such as those located at $tU_b/\delta \approx -8$ and -17, with both extending to $y/\delta \approx 0.4$. The structures present along the HMP, shown in figure 6c, appear to have longer streamwise extent than those situated along the LMP and appear to be more consistent with the character of smooth-wall flow.

To better visualize the modifications that multi-scale complex roughness introduces in the instantaneous structure of the flow, figure 7 provides a zoomed-in version of figure 6 with the addition of the other two fluctuating velocity components, v'/U_e and w'/U_e, together with the instantaneous RSS events, $u'v'/U_e^2$. Focusing on the stream-wise instantaneous events (first row in figure 7), significant structural modifications can be seen for the LMP and HMP cases, particularly for $y/\delta \leq 0.1$ where enhanced small-scale activity is noted in the two roughness cases compared to the smooth-wall flow. As mentioned previously, these events have a length scale consistent with that of the roughness and likely represent flow structures directly generated at the wall by the roughness. Furthermore, the larger-scale events depicted for the LMP case appear distinctly shorter in streamwise extent compared to those identified at the location of an HMP. As mentioned previously, a more significant alteration of this behavior is seen for the LMP case as highlighted in the zoomed-in figure. Significant structural modification is also apparent in the wall-normal fluctuating velocity, v', shown in the second row of figure 7. While the smooth-wall case reflects high degree in variability in v', the two rough-wall cases show more ordered occurrences of v' events in time as well as a larger-scale extent in the wall-normal direction. Similar behavior is identified in the spanwise fluctuating velocity, w', depicted in the third row of figure 7. Perhaps the most notable structural modifications by roughness are apparent in the instantaneous RSS events, shown in the fourth row of figure 7. Similar to all the individual fluctuating velocity components, roughness appears to introduce smaller-scale RSS events close to the rough surface, particularly along the LMP. In fact, for the structures visualized in this zoomed-in plot, the events along the LMP appear to be more significantly modified compared to smooth-wall flow than those along the HMP. This difference could indicate that at an LMP the roughness impact on the structural skeleton of smooth-wall flow penetrates deeper into the boundary layer, where at an HMP it is more confined to a region closer to the rough surface.

In order to quantitatively asses the impact of roughness on the LSMs and VLSMs present in the flow, specifically their TKE and RSS distribution across scales deep
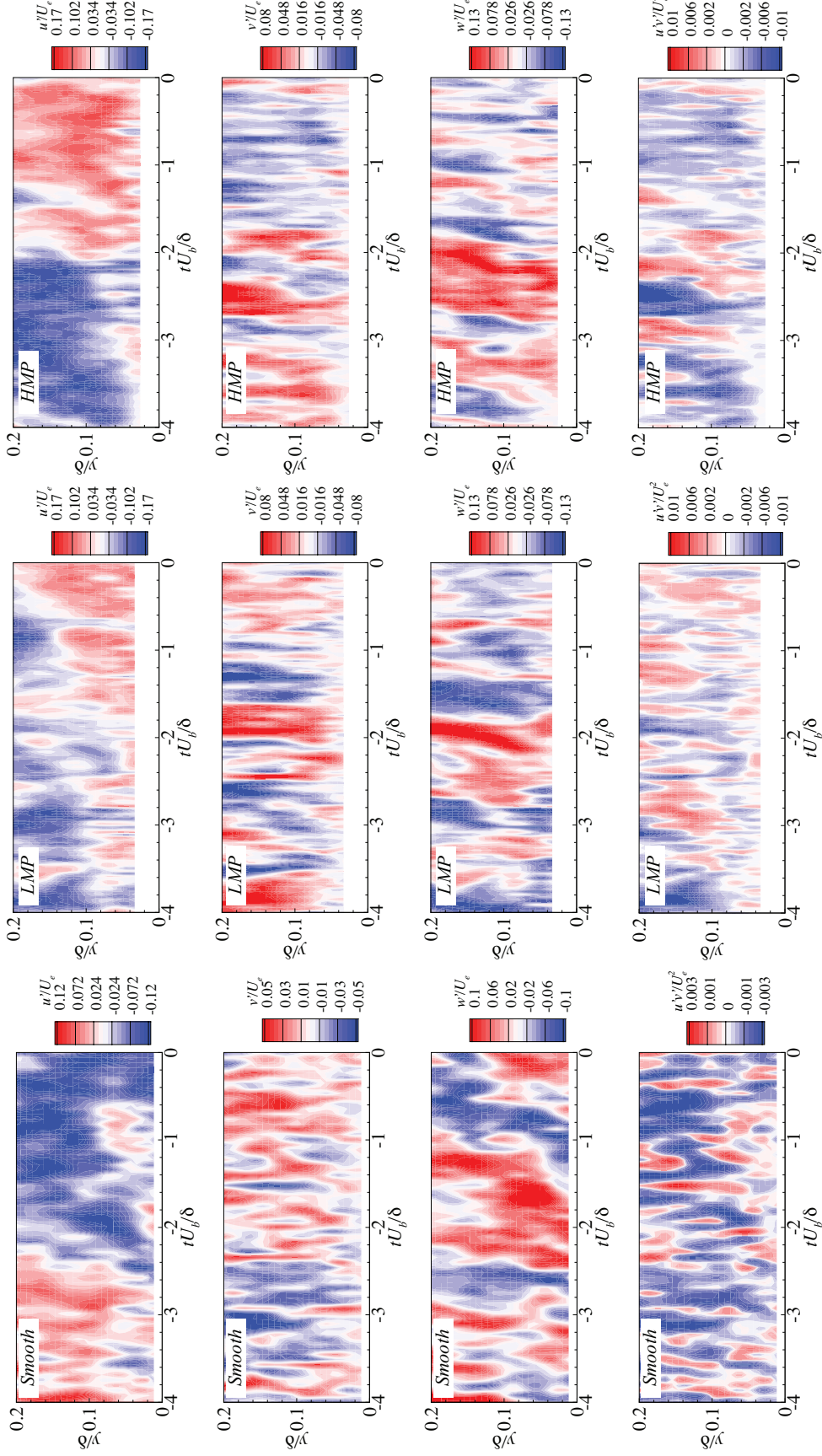
Figure 7. Time-height contours of fluctuating streamwise (first row), wall-normal (second row) and spanwise (third row) velocities as well as instantaneous Reynolds shear stress ($u'v'$; fourth row) for smooth-wall [43] (first column) and rough-wall flow at an LMP (second column) and HMP (third column). The time axis is normalized by the bulk velocity and the boundary-layer thickness to give a qualitative sense of the streamwise scales of the different structures identified.

15

within the roughness sublayer, premultiplied energy spectra were computed from the 10k fields/s data by extracting time series from the PIV fields. The total number of samples was 21,845, corresponding to a total time of $\approx 2.2\,\mathrm{s}$ which corresponds to $406\delta/U_e$. The individual power spectral density (PSD) of the velocity was computed using the Welch method, where the time-series signal was divided into 5 segments with 50% overlap to reduce the variance in the PSD. A Hanning window function was applied to each of the segments to suppress the Gibb's phenomenon at high frequencies [6]. Although great care was taken when performing the experiments, PIV data suffers from some degree of noise that can degrade the velocity spectra calculation. Vtel et al. [45] showed that the PIV noise is uncorrelated in time which significantly improves the efficiency of temporal denoising methods. In order to minimize this effect, all of the velocity time-series signals were denoised by a convolution of a narrow Gaussian filter with a standard deviation of $0.7\Delta t$. To assist in the convergence of the spectra, localized spanwise averaging was performed. For the smooth case [figure 8a] a spanwise average was perform over the full width of the domain, while for the spectra at the LMPs and HMPs a localized spanwise average over 4 mm intervals was performed (this corresponded to approximately the spanwise width of the larger roughness elements of the topography). To help further convergence, the rough-wall spectra were averaged over 5 independent runs. The uncertainty of the spectral estimation is $\approx 3\%$ for the smooth-wall, and $\approx 6\%$ for the rough-wall cases [43].

To estimate wavenumber spectra, Taylor's frozen-field hypothesis was use to convert frequency to streamwise wavenumber. Ideally, true spatial spectra should always be used to provide an unambiguous view of these physics. However, the fields of view possible with PIV systems still cannot compare to the temporal record length of hot-wire systems, for example, meaning the latter must be used to access the larger scales of the flow. We recognize that while there could exist small errors in the peak locations of the premultiplied spectra using Taylor's hypothesis for rough-wall flows [46], the overall shape of the spectra is not changed. Additionally, although the validity of the Taylor's hypothesis to accurately determine the true spatial spectra is still a subject of debate [5,36,47], it has little impact on the observations reported herein since, as point out by Guala et al. [6], the time-delayed correlations decay faster than the two-point correlations due to the evolution of the turbulent structures as they advect through the PIV measurement plane. Thus, the streamwise wavenumber determined as $k_x = 2\pi f/U(y)$, where $U(y)$ is the local mean velocity at the wall-normal location, and the streamwise wavelength was computed as $\lambda_x = 2\pi/k_x$, will reveal less energy at low wavenumbers compared to the true spatial spectrum. Therefore, since the main goal of the present effort is to determine the fractional content of both TKE and RSS that reside at low wavenumbers and are associated with LSMs and VLSMs, the errors involved with Taylor's hypothesis and convection velocities are not appreciable enough to impact these goals.

Premultiplied spectra of the streamwise velocity, $k_x\phi_{uu}$ for all of the examined cases (smooth, LMP and HMP) are presented in figure 8. As noted in Balakumar and Adrian [7], premultiplied spectra are useful to clearly present the contribution of the different wavelengths to the spectra and to locate peaks in the spectral densities. All of the spectra shown herein were normalized using quantities determined from ensemble-averaged followed by spanwise-averaged velocity profiles, where δ was determined 99% of the free stream velocity and u_τ from the plateau value from $u_\tau = \sqrt{\nu\partial\langle U\rangle/\partial y - \langle u'v'\rangle}$.

The smooth-wall premultiplied spectra with outer-flow scaling, illustrated in figure 8(a), reflect the expected double-peak structure that was reported in many previous
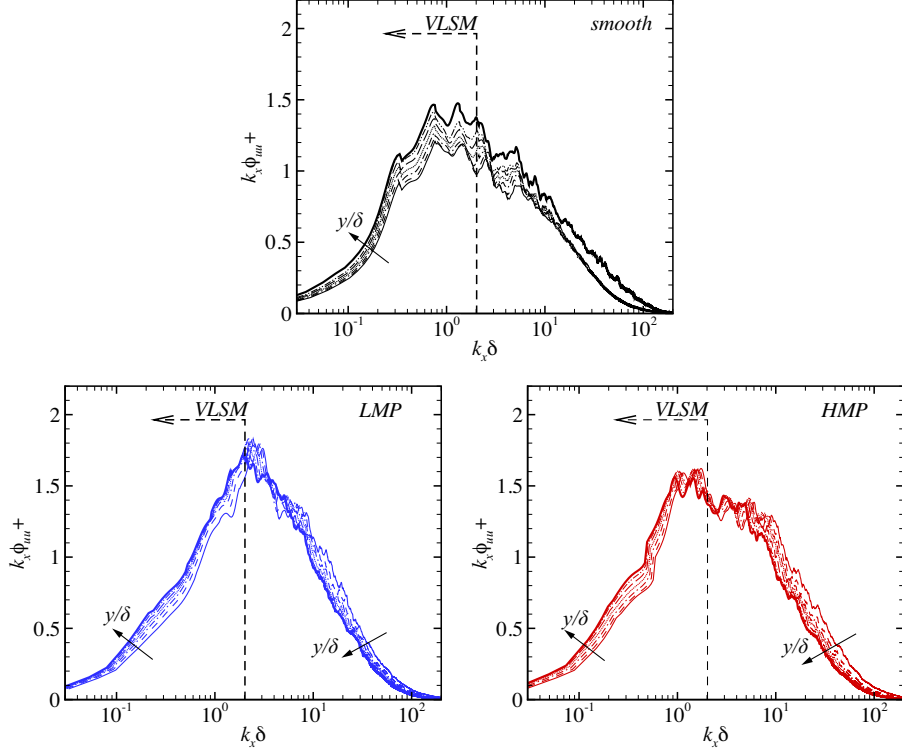
Figure 8. Premultiplied streamwise velocity spectra, $k_x\phi_{uu}{}^+$, as a function of streamwise wavenumber, $k_x\delta$, for (a) smooth-wall flow and rough-wall flow along an (b) LMP and an (c) HMP. Dash vertical line demarcates the VLSM boundary ($k_x\delta < 2$). (——), $y/\delta = 0.032$; (— —), $y/\delta = 0.045$; (—.—), $y/\delta = 0.052$; (··), $y/\delta = 0.060$; (— —), $y/\delta = 0.068$; (—··), $y/\delta = 0.075$; (——), $y/\delta = 0.082$.

works [5,7,11]. These peaks correspond to the energy of the VLSM ($\approx 6\delta$) and LSM ($\approx 1\delta$) structures. Here, we follow the same convention as Balakumar and Adrian [7] and Guala et al. [6] to distinguish the VLSMs from the LSMs, specifically utilizing a dividing line at $k_x\delta = 2$, which is demarcated by the vertical dashed lines in figure 8. Of interest, Kim and Adrian [5] interpreted this double-peak structure as the organization of hairpin-like vortices into large- and very large-scale motions, with the peak at $\lambda \approx 1\delta$ ($k_x\delta \approx 2\pi$) corresponding to individual hairpin vortex packets and the peak at $\lambda_x \approx 6\delta$ ($k_x\delta \approx 1$) to the alignment of these packets into streamwise-elongated trains of packets. In this outer-scale representation, the spectra show an increase of energy associated with VLSMs as a function of wall-normal position, consistent with previous studies [5,7]. These smooth-wall results are utilized as a baseline against which the rough-wall results are compared.

Figure 8(b) presents pre-multiplied streamwise velocity spectra at a spanwise location coincident with an LMP in the mean velocity field. Alternations are noted in these spectra acquired at the LMP, where the results suggest a shift of VLSM energy to smaller scales that are closer in wavelength to LSMs. In particular, there is a distinct peak at $k_x\delta \approx 2$, suggesting a concentration of u' energy in structures of scale $\lambda_x \approx 3\delta$. This trend of VLSM-scale energy shifting to shorter streamwise wavelengths coincident with an LMP is entirely consistent with that reported by Pathikonda and Christensen [30] from hot-wire measurements over the same complex roughness as well as the LES results of Awasthi and Anderson [31] for flow over a simplified, spanwise-varying topography that also formed turbulent secondary flows. Moreover, in this

17

outer-scale representation, the results suggest that further way from the wall the energy of the high-wavenumber streamwise scales, $k_x\delta > 2$ diminishes. On the other hand, the opposite behavior is seen for the low-wavenumber scales, $k_x\delta < 2$, where the energy content of these scales increases as a function of wall-normal position. It is worth mentioning once more that these measurements were taken deep within the roughness sublayer and so they reflect the behavior of the flow in the vicinity of the rough surface.

The premultiplied streamwise velocity spectra coincident with an HMP, shown in figure 8(c), show different trends than those noted coincident with the LMP. These spectra reflect a bimodal distribution, similar to that of the smooth-wall spectra (figure 8a), with distinct concentrations of energy at $\lambda_x \approx 6\delta$ ($k_x\delta \approx 1$) and $\lambda_x \approx 1.5\delta$ ($k_x\delta \approx 4$). This behavior suggests the presence of both VLSMs and LSMs along HMPs, whereas the VLSM energy appears shifted towards shorter streamwise wavelengths towards that of LSMs along the LMP which only embodies a clear peak in energy at $\lambda_x \approx 3\delta$ ($k_x\delta \approx 2$). Again, these results reflect the same trends reported by Pathikonda and Christensen [30] from hot-wire measurements over the same roughness, but are in contrast to the reported annihilation of VLSMs coincident to an HMP in the work of Awasthi and Anderson [31]. As mentioned earlier, this behavior is observed deep within the roughness sublayer. The LES simulations from Awasthi and Anderson [31] may embody different boundary conditions inside the roughness sublayer at HMPs due to the simplified nature of the spanwise-varying topography. Nonetheless, the locations of the LMPs and HMPs with respect to topographical features of the roughness matches with this work. It should be noted that different roughness configurations can lead to differences in the secondary motions as seen in Vanderwel and Ganapathisubramani [29], where an opposite behavior of the locations of the LMPs and HMPs with respect to the roughness topography was seen.In addition, a similar behavior regarding the energy of the low- and high-wavenumber scales as a function of wall-normal position as was noted at the LMP is also noted at the HMP. Finally, the energy at scales higher than $k_x\delta > 2$ decreases with wall-normal distance, and for scales less than $k_x\delta$ their energy increases with wall-normal distance.

Figure 9 presents premultiplied wall-normal velocity spectra for the smooth, LMP and HMP cases. In contrast to the premultiplied streamwise velocity spectra where a significant fraction of the energy resides at large scales, the wall-normal contributions to TKE reside predominantly at small scales as noted in the smooth-wall spectra (figure 9a). In particular, a distinct peak is noted for all wall-normal positions, with the peak position varying from $\approx 35k_x\delta$ near the wall to $\approx 20k_x\delta$ further from the wall. In addition, the energy of the low-wavenumber wall-normal scales increases as a function of wall-normal position. Both the LMP and HMP cases (figures 9b and c, respectively) display similar behavior as the smooth-wall flow; however, for these cases, roughness introduces a greater wall-normal dependency. In addition, the position of the peak close to the roughness occurs at higher wavenumbers: $\approx 40k_x\delta$ for the LMP and $\approx 50k_x\delta$ for the HMP. Thus, roughness enhances v' contributions to TKE close to the wall, particularly at smaller scales. Further from the wall, both roughness cases show the peak in the spectrum moving to a wavenumber closer to the smooth-wall result. Additionally, these shift of the peak of the wall-normal premultiplied spectra towards lower wavenumbers as a function of wall-normal distance was recently seen in Squire et al. [46] for both smooth- and rough-wall flows.

The nature of the present high-speed stereo PIV measurements also allowed the calculation of premultiplied spanwise velocity spectra, $k_x\phi_{ww}{}^+$, for the smooth-wall, LMP and HMP cases as shown in figure 10. The spectra for all three cases embody
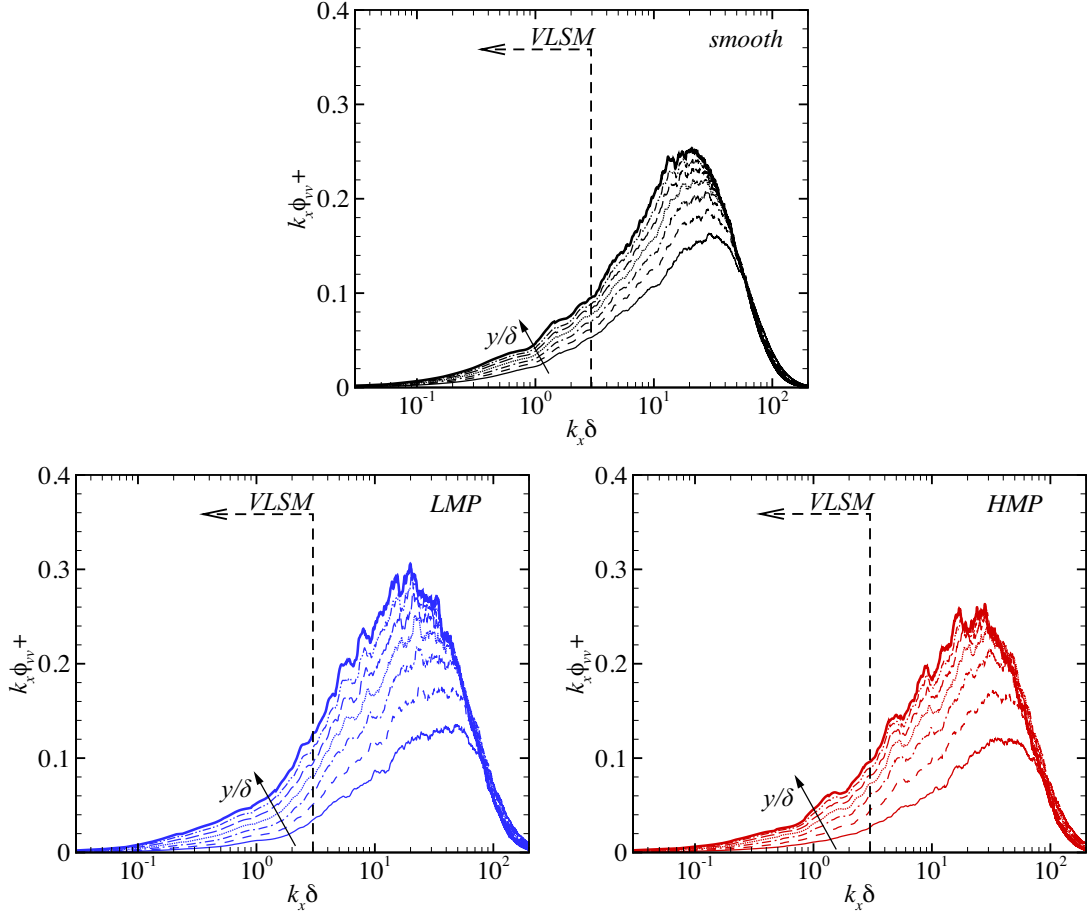
Figure 9. Premultiplied wall-normal velocity spectra, $k_x\phi_{vv}{}^+$, as a function of streamwise wavenumber, $k_x\delta$, for (a) smooth-wall flow and rough-wall flow along an (b) LMP and an (c) HMP. Dash vertical line demarcates the VLSM boundary ($k_x\delta < 2$). For line legend, see figure 8.

peaks at $\approx 10k_x\delta$ for all wall-normal positions shown. However, in the vicinity of the peak, the smooth-wall spectra display a higher degree of wall-normal dependence than is observed in the LMP and HMP cases. Interestingly, the opposite behavior is seen for lower wavenumbers for both the LMP and HMP cases when compared with the smooth-wall result. For the smooth-wall case, although small but apparent, the energy of the lower wavenumbers is proportional to the wall-normal position. However, the opposite is seen for both the HMP and LMP cases, where the energy content of the lower wavenumbers is inversely proportional to wall-normal position.

Finally, figure 11 presents the premultiplied co-spectra, $k_x\phi_{uv}{}^+$. The smooth-wall co-spectra, figure 11(a), show significant $u'v'$ content at larger scales (lower wavenumbers) as previously reported by Balakumar and Adrian [7], Guala et al. [6] The LMP and HMP cases, depicted in figure 11(b) and (c), respectively, show very different behavior when compared with the smooth-wall co-spectra. Focusing first on larger scales, similar to that noted for $k_x\phi_{uu}{}^+$, a bimodal distribution is noted in the smooth-wall result reflective of RSS content embodied by VLSMs and LSMs. In contrast, and again similar to that noted for $k_x\phi_{uu}{}^+$, this lower wavenumber RSS content shifts to shorter streamwise wavelengths along the LMP. An even more drastic reduction in RSS content of VLSMs is noted along the HMP and the shift in RSS content to shorter streamwise
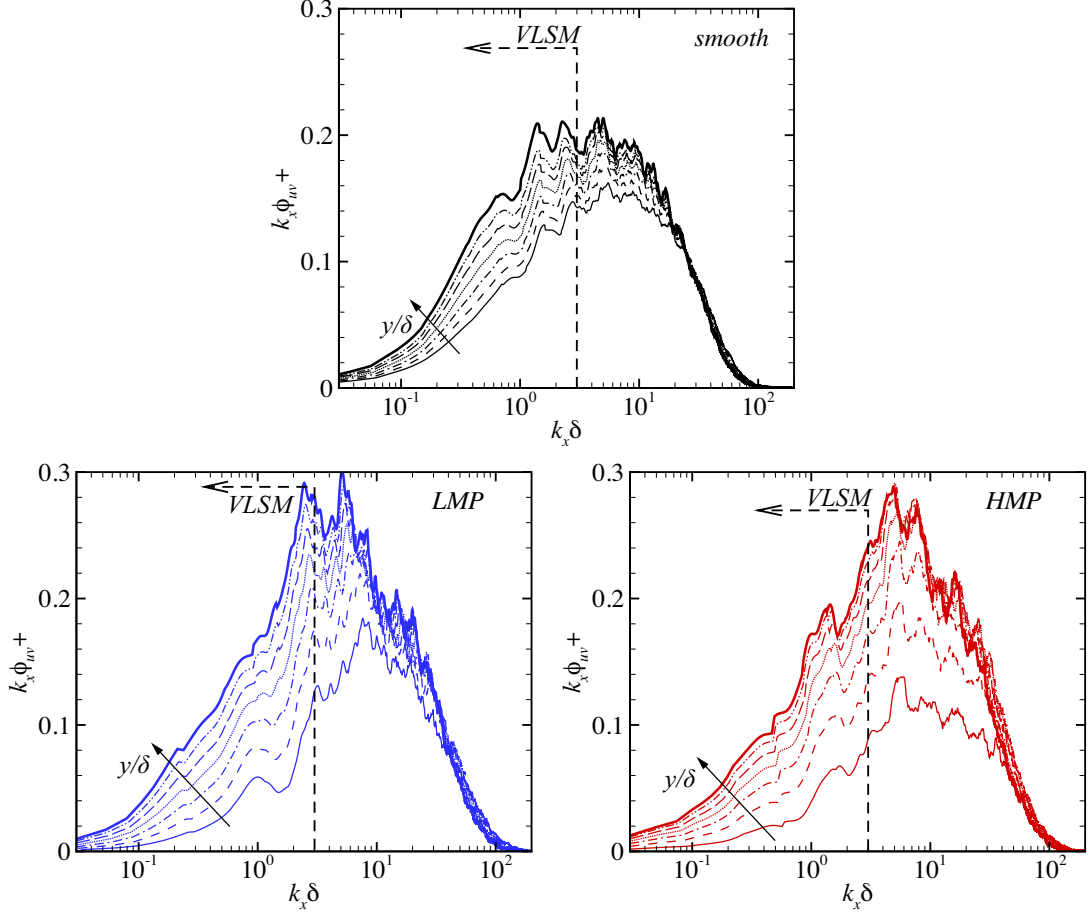
19
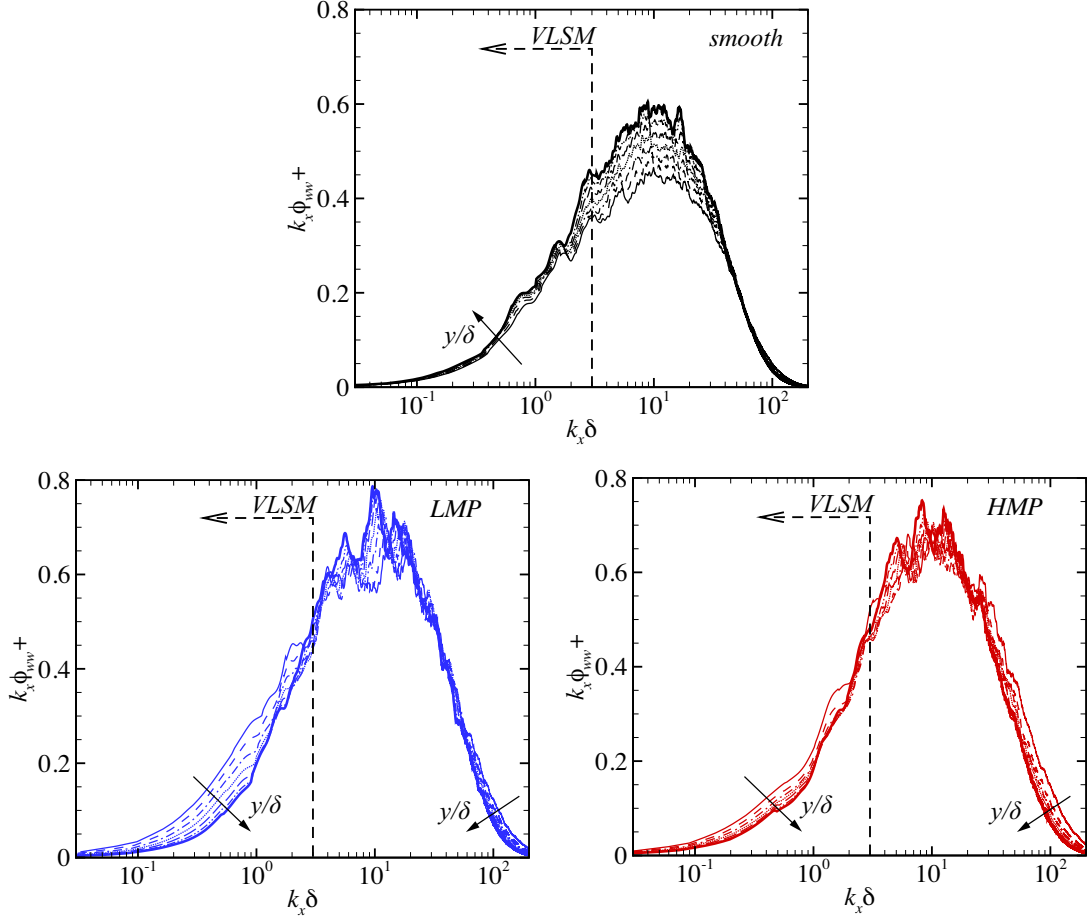
Figure 10. Premultiplied spanwise velocity spectra, $k_x \phi_{ww}{}^+$, as a function of streamwise wavenumber, $k_x \delta$, for (a) smooth-wall flow and rough-wall flow along an (b) LMP and an (c) HMP. Dash vertical line demarcates the VLSM boundary ($k_x \delta < 2$). For line legend, see figure 8.

scales is even more evident compared to the LMP results. Furthermore, the HMP and LMP cases show drastically enhanced wall-normal dependence compared to smooth-wall flopw. Close to the wall, the peak in the co-spectra for both the LMP and HMP cases resides at smaller scales ($\approx 8k_x \delta$ for the LMP case; $\approx 5k_x \delta$ for the HMP case), and this peak location shifts towards lower wavenumbers with increasing wall-normal location until a peak location comparable to the smooth-wall result is observed. This result highlights the drastic influence of roughness on the smaller scales of the flow and perhaps also its influence in suppressing aspects of the larger-scale motions (VLSMs and LSMs).

To determine the TKE and RSS content as a function of scale (i.e., for the different streamwise wavelengths) for the smooth, LMP and HMP cases investigated herein, cumulative distributions of TKE and RSS from all wavenumbers were calculated as
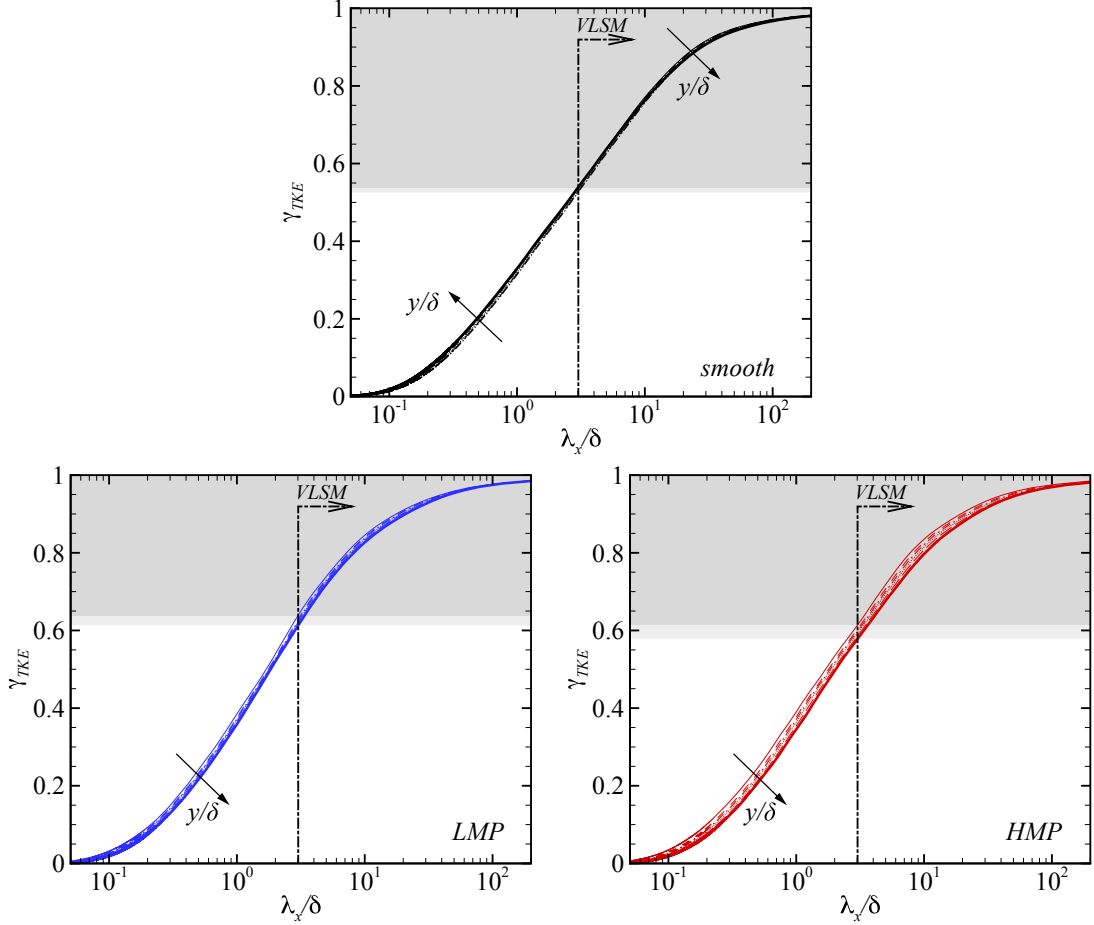
$$\gamma_{ij}(\lambda_x) = 1 - \frac{\sum_0^k \phi_{ij}(k_x)\Delta k_x}{\sum_0^{k_{max}} \phi_{ij}(k_x)\Delta k_x}. \tag{1}$$

Figure 12 presents the cumulative TKE distribution as a function of streamwise wavelength, λ_x, for various wall-normal locations. Here, the cumulative TKE is computed

20

Figure 11. Premultiplied co-spectra, $k_x\phi_{uv}{}^+$, as a function of streetwise wavelength, $k_x\delta$, for (a) smooth-wall flow and rough-wall flow along an (b) LMP and an (c) HMP. Dash vertical line demarcates the VLSM boundary ($k_x\delta < 2$).. For line legend, see figure 8.

using the velocity spectra from all three fluctuating velocity components and thus embodies the full TKE contribution. For the smooth-wall case, shown in figure 12(a), the VLSMs (scales larger than 3δ) account for approximately 45% of the TKE. This result is consistent with Balakumar and Adrian [7]. Roughness reduces the overall TKE content of the VLSMs and also introduces a more apparent wall-normal dependence when compared to the smooth-wall case, as can be seen for both the LMP and HMP cases (figures 12b) and c, respectively). Similar to the streamwise velocity spectra behavior, the cumulative TKE distribution at an LMP shows noted differences when compared with the smooth-wall and HMP results, with a reduction in the TKE content of the VLSMs to 35-40% (see gray shading in figure 12(b)). Consequently, scales smaller than VLSMs become relatively more energetic along the LMP compared to smooth-wall flow. This trend, although small, is consistent with that noted by Awasthi and Anderson [31] for flow along an LMP based on analysis of streamwise velocity contributions to the TKE. In contrast to Awasthi and Anderson [31], however, the overall TKE content of VLSM scales at the HMP is approximately 40-43%, which is roughly the same as that of smooth-wall flow for the present complex roughness case. Finally, both rough-wall cases display a slightly higher wall-normal dependency of the TKE content when compared with the smooth-wall case. This dependence is more apparent

Figure 12. Cumulative TKE distribution as a function of streamwise scale for (a) smooth-wall flow and rough-wall flow at an (b) LMP and an (c) HMP. Dash line demarcates the VLSM ($\lambda/\delta > 3$). For line legend, see figure 8. Gray shaded areas illustrate the wall-normal range of TKE content in VLSMs.

at an HMP, which suggests a variation of the TKE content of the VLSMs as a function of wall-normal distance.

Figure 13 presents the cumulative RSS distribution as a function of streamwise wavelength. For the smooth-wall case, shown in figure 13(a), trends very similar to those of Balakumar and Adrian [7] are noted, with the RSS content at the scales of VLSMs having strong wall-normal dependence, varying from 35% (close to the wall) to 45% (further from the wall). As expected from the premultiplied co-spectra presented in figure 11, the RSS content of VLSMs is smaller for rough-wall flow. At an LMP, the RSS content of the VLSMs, depicted in figure 13(b), ranges from less than 20% close to the wall to 40% further from the wall. Thus, as with the noted shift in TKE to smaller streamwise scales in the cumulative TKE, here the RSS content primarily resides at scales smaller than that which occurs in smooth-wall flow. At an HMP, the RSS content associated with VLSMs is also approximately 20% very close to the roughness, but increases less rapidly than that for the LMP with increasing wall-normal distance to 30-35%. Despite these differences away from the wall, both the LMP and HMP cases reflect a dramatic shift in RSS content to scales much smaller than VLSMs and LSMs which is likely the result of energetic, smaller-scale motions generated by the roughness itself.

22
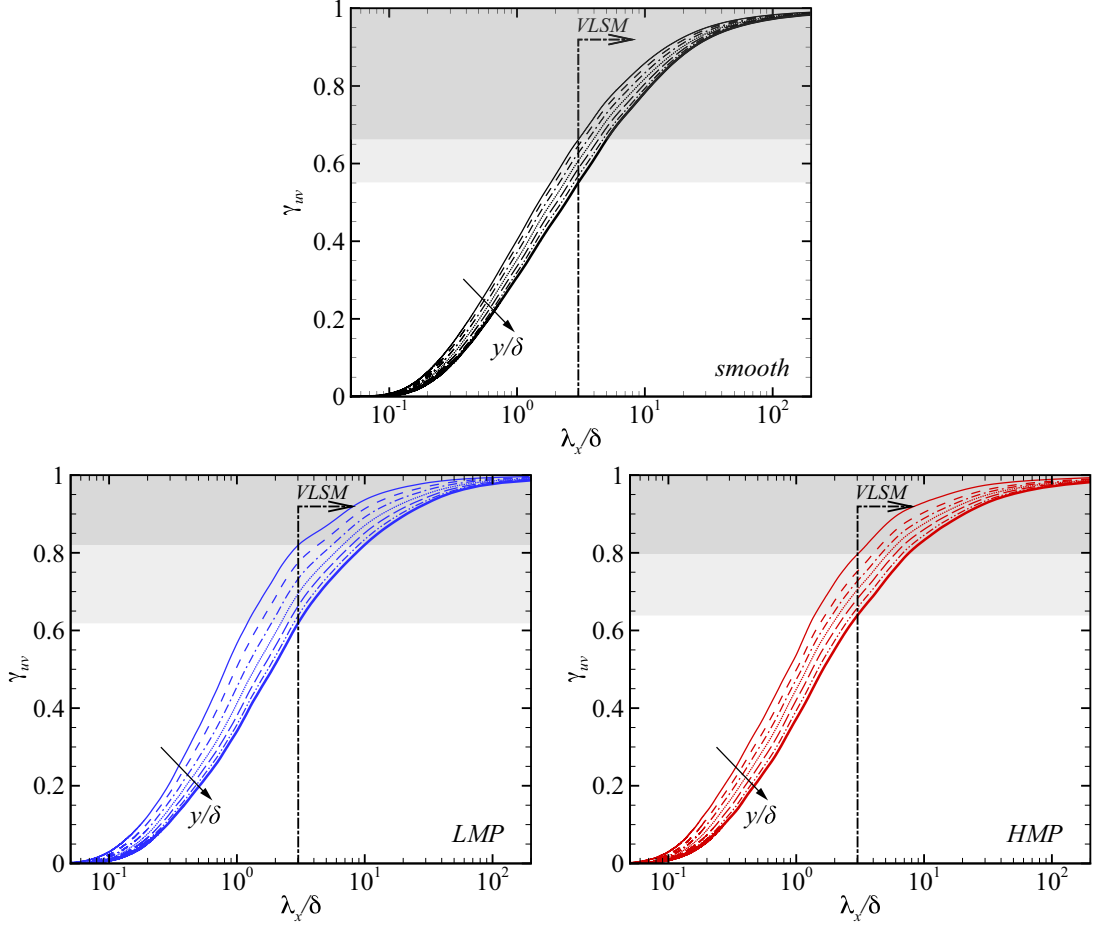
Figure 13. Cumulative RSS distribution as a function of streamwise scale for (a) smooth-wall flow and rough-wall flow at an (b) LMP and an (c) HMP. Dash line demarcates the VLSM ($\lambda_x/\delta > 3$). For line legend, see figure 8. Gray shaded areas illustrate the wall-normal range of RSS content in VLSMs.

In a previous effort, Anderson et al. [25] found that secondary motions are sustained via roughness-induced spanwise heterogeneities in the Reynolds stresses, which causes an imbalance between the production and dissipation of TKE. As these secondary motions are strongest in the roughness sublayer, the reduction in TKE and RSS content in VLSMs, particularly at LMPs, might be a byproduct of these secondary motions.

4. Summary

High-frame-rate stereo PIV was employed to capture the time-dependent flow in the spanwise–wall-normal (y, z) plane deep within the roughness sublayer of a turbulent boundary layer overlying complex roughness. Previous results from Barros and Christensen [1] revealed that this roughness topography introduces spanwise heterogeneities in the mean flow in the form of low- and high-momentum pathways that are flanked by counter-rotating swirling motions–now known to be the imprint of roughness-induced turbulent secondary flows [25]. The present data was utilized to study the impact of roughness on the TKE and RSS content of the larger scales of the flow, principally LSMs and VLSMs.

23

Taylor's hypothesis reconstructions of streamwise elongated fields of view highlight the presence of long, meandering motions consistent with that previously identified in smooth-wall flow by Hutchins and Marusic [10] which are known to embody a significant fraction of the TKE and RSS. In the case of roughness, time-history plots as a function of wall-normal position coincident with the aforementioned LMP and HMP patterns associated with the roughness-induced secondary flows revealed significant modification of the TKE and RSS content of these motions. In particular, premultiplied spectra of streamwise velocity revealed a shift of VLSM energy to shorter streamwise wavelengths along an LMP into a single peak at $\lambda_x \approx 3\delta$ ($k_x\delta \approx 2$) and the disappearance of the bimodal distribution noted in similar smooth-wall streamwise velocity spectra that reflect the impact of VLSMs and LSMs. In contrast, this bimodal distribution remains intact at an HMP, with peaks at $\lambda_x \approx 1.5$ and $\lambda_x \approx 6$ ($k_x\delta \approx 4$ and $k_x\delta \approx 1$, respectively). Cumulative TKE distributions as a function of scale confirm a shift in overall TKE content to shorter streamwise wavelengths at LMP compared to smooth-wall flow and at an HMP. Finally, roughness significantly alters the distribution of RSS as a function of scale. Very close to the rough wall, most RSS content resides at scales comparable to the roughness, compared to 35% of the RSS content residing at VLSM scales. This peak in RSS content shifts to larger scales with increasing wall-normal location, though the RSS content of VLSMs at an HMP (30-35%) and an LMP (40%) are still reduced when compared with smooth-wall flow (45%).

5. Acknowledgements

References

[1] Barros JM, Christensen KT. Observations of turbulent secondary flows in a rough-wall boundary layer. J Fluid Mech. 2014;748.

[2] Townsend A. The turbulent boundary layer. In: Grenzschichtforschung/boundary layer research. Springer; 1958. p. 1–15.

[3] Grant H. The large eddies of turbulent motion. J Fluid Mech. 1958;4(02):149–190.

[4] Adrian RJ, Meinhart CD, Tomkins CD. Vortex organization in the outer region of the turbulent boundary layer. J Fluid Mech. 2000;422:1–54.

[5] Kim KC, Adrian RJ. Very large-scale motion in the outer layer. Phys Fluids. 1999;11:417–422.

[6] Guala M, Hommema SE, Adrian RJ. Large-scale and very-large-scale motions in turbulent pipe flow. J Fluid Mech. 2006;554:521–542.

[7] Balakumar BJ, Adrian RJ. Large- and very-large-scale motions in channel and boundary-layer flows. Philos T R Soc A. 2007;365:665–681.

[8] Monty J, Hutchins N, Ng H, et al. A comparison of turbulent pipe, channel and boundary layer flows. J Fluid Mech. 2009;632:431–442.

[9] Kunkel GJ, Marusic I. Study of the near-wall-turbulent region of the high-Reynolds-number boundary layer using an atmospheric flow. J Fluid Mech. 2006;548:375–402.

[10] Hutchins N, Marusic I. Evidence of very long meandering features in the logarithmic region of turbulent boundary layers. J Fluid Mech. 2007;579:1–28.

[11] Mathis R, Hutchins N, Marusic I. Large-scale amplitude modulation of the small-scale structures in turbulent boundary layers. J Fluid Mech. 2009;628:311.

[12] Mathis R, Monty J, Hutchins N, et al. Comparison of large-scale amplitude modulation in turbulent boundary layers, pipes, and channel flows. Phys Fluids. 2009;21:111703.

[13] Bandyopadhyay PR, Hussain A. The coupling between scales in shear flows. Physics of Fluids (1958-1988). 1984;27(9):2221–2228.

[14] Krogstad PA, Antonia RA, Browne LWB. Comparison between rough and smooth-wall turbulent boundary layers. J Fluid Mech. 1992;245:599–617.

[15] Krogstad PA, Antonia RA. Surface roughness effects in turbulent boundary layers. Exp Fluids. 1999;27:450–460.

[16] Volino RJ, Schultz MP, Flack KA. Turbulence structure in rough- and smooth-wall boundary layers. J Fluid Mech. 2007;592:263–293.

[17] Wu Y, Christensen KT. Outer-layer similarity in the presence of a practical rough-wall topography. Phys Fluids. 2007;19:085108.

[18] Wu Y, Christensen KT. Spatial structure of a turbulent boundary layer with irregular surface roughness. J Fluid Mech. 2010;655:380–418.

[19] Volino RJ, Schultz MP, Flack KA. Turbulence structure in a boundary layer with two-dimensional roughness. J Fluid Mech. 2009;635:75–101.

[20] Allen J, Shockling M, Kunkel G, et al. Turbulent flow in smooth and rough pipes. Philos T R Soc A. 2007;365(1852):699–714.

[21] Monty J, Allen J, Lien K, et al. Modification of the large-scale features of high reynolds number wall turbulence by passive surface obtrusions. Exp Fluids. 2011;51(6):1755–1763.

[22] Jacobi I, McKeon B. New perspectives on the impulsive roughness-perturbation of a turbulent boundary layer. J Fluid Mech. 2011;677:179–203.

[23] Pathikonda G. Structure of turbulent channel flow perturbation by cylindrical roughness elements [master's thesis]. University of Illinois at Urbana-Champaign; 2013.

[24] Mejia-Alvarez R, Barros JM, Christensen KT. Structural attributes of turbulent flow over a complex topography. Wiley-Blackwell; 2013. Chapter 3; p. 25–41.

[25] Anderson W, Barros JM, Christensen KT. Numerical and experimental study of mechanisms responsible for turbulent secondary flows in boundary layer flows over spanwise heterogeneous roughness. J Fluid Mech. 2015;748:316–347.

[26] Vermaas DA, Uijttewall WSJ, Hoitink AJF. Lateral transfer of streamwise momentum caused by a roughness transition across a shallow channel. Water Resour Res. 2011; 47:W02530.

[27] Nugroho B, Hutchins N, Monty JP. Large-scale spanwise periodicity in a turbulent boundary layer induced by highly ordered and direction surface roughness. Int J Heat Fluid Fl. 2013;41:90–102.

[28] Willingham D, Anderson W, Christensen KT, et al. Turbulent boundary layer flow over transverse aerodynamics roughness transitions: induced mixing and flow characterization. Phys Fluids. 2014;26:021402.

[29] Vanderwel C, Ganapathisubramani B. Effects of spanwise spacing on large-scale secondary flows in rough-wall turbulent boundary layers. J Fluid Mech. 2015;774:R2.

[30] Pathikonda G, Christensen KT. Inner–outer interactions in a turbulent boundary layer overlying complex roughness. Physical Review Fluids. 2017;2(4):044603.

[31] Awasthi A, Anderson W. Numerical study of turbulent channel flow perturbed by spanwise topographic heterogeneity: Amplitude and frequency modulation within low-and high-momentum pathways. Physical Review Fluids. 2018;3(4):044602.

[32] Mejia-Alvarez R, Christensen KT. Low-order representations of irregular surface roughness and their impact on a turbulent boundary layer. Phys Fluids. 2010;22(1):015106–015106.

[33] Mejia-Alvarez R, Christensen KT. Wall-parallel stereo particle-image velocimetry measurements in the roughness sublayer of turbulent flow overlying highly irregular roughness. Phys Fluids. 2013;25(11):115109.

[34] Bons JP, Taylor RP, McClain ST, et al. The many faces of turbine surface roughness. J Turbomach. 2001;123:739–748.

[35] Soloff SM, Adrian RJ, Liu ZC. Distortion compensation for generalized stereoscopic par-

ticle image velocimetry. Meas Sci Technol. 1997;8(1441-1454).

[36] Dennis DJ, Nickels TB. On the limitations of taylor's hypothesis in constructing long structures in a turbulent boundary layer. J Fluid Mech. 2008;614:197.

[37] Dennis DJ, Nickels TB. Experimental measurement of large-scale three-dimensional structures in a turbulent boundary layer. part 1. vortex packets. J Fluid Mech. 2011;673:180–217.

[38] Van Doorne C, Westerweel J. Measurement of laminar, transitional and turbulent pipe flow using stereoscopic-piv. Exp Fluids. 2007;42(2):259–279.

[39] Hutchins N, Marusic I. Large-scale influences in near-wall turbulence. Philos T R Soc A. 2007;365(1852):647–664.

[40] Rohaly J, Frigerio F, Hart D. Reverse hierarchical piv processing. Meas Sci Technol. 2002; 13:984.

[41] Townsend AA. The structure of turbulent shear flow. 2nd ed. Cambridge University Press; 1976.

[42] Mejia-Alvarez R, Wu Y, Christensen K. Observations of meandering superstructures in the roughness sublayer of a turbulent boundary layer. Int J Heat Fluid Fl. 2014;48:43–51.

[43] Barros JM. Cross-plane stereo-piv measurements of a turbulent boundary layer over highly irregular roughness [dissertation]. University of Illinois at Urbana-Champaign; 2014.

[44] Christensen KT, Adrian RJ. Statistical evidence of hairpin vortex packets in wall turbulence. J Fluid Mech. 2001;431:433–443.

[45] Vétel J, Garon A, Pelletier D. Denoising methods for time-resolved piv measurements. Exp Fluids. 2011;51(4):893–916.

[46] Squire D, Hutchins N, Morrill-Winter C, et al. Applicability of taylor's hypothesis in rough-and smooth-wall boundary layers. J Fluid Mech. 2017;812:398–417.

[47] Del Alamo JC, Jiménez J. Estimation of turbulent convection velocities and corrections to taylor's approximation. J Fluid Mech. 2009;640:5–26.